Advances in Colloid and Interface Science 270 (2019) 73–86

Contents lists available at ScienceDirect

Advances in Colloid and Interface Science

journal homepage: www.elsevier.com/locate/cis

Historical perspective

Controlling the lifetime of antibubbles

Youen Vitry [a], Stéphane Dorbolo [b], Jan Vermant [c], Benoit Scheid [a,*]

[a] TIPS C.P.165/67, Université Libre de Bruxelles, Av. F. Roosevelt 50, 1050 Brussels, Belgium
[b] GRASP, Physics Department, Building B5a, Sart-Tilman, University of Liège, B4000 Liège, Belgium
[c] ETH Zürich, Dept. of materials, Vladimir-Prelog-Weg 5, CH-8093 Zürich, Switzerland

ARTICLE INFO

Article history:
16 May 2019
Available online 25 May 2019

Keywords:
Surfactants
Antibubbles
Drainage
Surface viscosity
Surface elasticity

ABSTRACT

An antibubble is a liquid droplet wrapped by a thin layer of gas, inside a bulk liquid usually of the same composition. The lifetime of an antibubble is governed by the drainage of the gas between the two liquid-gas interfaces populated by surfactants. Depending on the relative magnitude of surface viscosity and elastic moduli, which directly depend on or are determined by the nature of surfactants, the lifetime of an antibubble may vary a lot, from few seconds to few minutes. While such a difference can be predicted with models that include the role of interfacial properties, they were not observed experimentally in previous studies, due to important sources of dispersion. In this review, the main sources of dispersion are identified, such as (i) the initial amount of gas embedded in the antibubble, (ii) the level of saturation of gas in the bulk liquid, (iii) the presence of dust particles (<0.5 μm) in the gas, and (iv) three-dimensional flow effects. By accounting for these various effects, we obtain a coherent view on the lifetime of an antibubble, as a function of its radius and the surface rheology, with excellent consistency between experiments and modeling. Results thus demonstrate that controlling the size and lifetime of antibubbles is achievable.

Contents

* Corresponding author.
E-mail address: bscheid@ulb.ac.be (B. Scheid).

https://doi.org/10.1016/j.cis.2019.05.007
0001-8686/

1. Introduction

The antibubble owns its name for being the opposite of a soap bubble. If a soap bubble is a thin spherical shell of soapy liquid surrounded by air, an antibubble is a thin spherical shell of air surrounded by liquid, as illustrated in Fig. 1. Antibubbles have first been reported in a scientific article by Hughes and Hughes in 1932 [1]. Even though antibubbles are extremely easy to make for an amateur scientist, as nicely described in 1974 by Stong [2], not much evidences exist on the presence of antibubbles in nature. During the 80's in the context of boiling, Ida and Takashima [3] and Nosoko and Mori [4] formed antibubbles, without naming it, by dropping a denser volatile liquid onto a surface of another hot liquid. Noticeably, it has recently been suggested that leaks from subsea hydrocarbon production facilities contain antibubbles with a specific acoustic signature [5]. Nowadays, benefiting from the development of microfluidics, several potential applications have arisen, such as using antibubbles as contrast agent for enhancing ultrasonic imaging [6,7] or loading the antibubble core with a ferrofluid to serve as a vehicle for magneto-controlled drug delivery [8].

Several configurations have been proposed to produce antibubbles. The most classical one being a jet impacting a liquid surface and entraining a gas layer into a liquid bath, the antibubble resulting from the destabilization of the air-wrapped jet inside the liquid bath [9,10]. Alternatively, Tufaile and Sarterelli [11] described the formation of an antibubble as a result of a complex coalescence process between two rising bubbles formed from a submerged nozzle: as the second bubble coalesces with the first one, a spike of liquid penetrates into the first bubble, and destabilizes by inverted dripping into a droplet, forming the antibubble. Postema et al. [12] produced micrometer-size antibubbles by a similar mechanism of ultrasound-induced coalescence of microbubbles. Poortinga [13] and Silpe et al. [14] proposed a method to prepare micro-antibubbles by a two-step approach: a core-shell water-in-oil-in-water emulsion is first generated *via* microfluidics and freeze-dried thereafter to yield, upon subsequent reconstitution, an aqueous dispersion of antibubbles. Recently, Shen et al. [15] generated antibubbles at the outlet of a capillary dipped into a liquid and from which a Taylor flow is exiting: the antibubble is produced as a result of the breakup of the liquid column formed into the preceding bubble

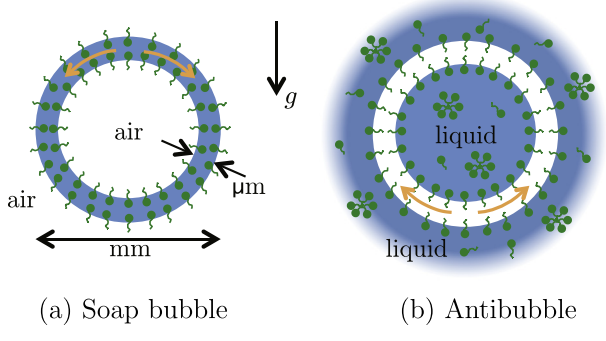

Fig. 1. Sketches of a soap bubble and an antibubble. Indicated typical dimensions in (a) are similar for (b). Surfactants are represented in green with their hydrophilic heads in the liquid and their hydrophobic tails in the air. The orange arrows indicate the direction of drainage under the action of gravity, *g*, in the liquid film (a) and in the air shell (b). (For interpretation of the references to colour in this figure legend, the reader is referred to the web version of this article.)

while still pinned at the tip of the capillary. Bai et al. [16] succeeded to produce antibubbles by shooting a liquid droplet onto a soap film, wrapping the drop with a shell of air: as the air-wrapped droplet reaches the liquid bath the external soap film coalesces with the surrounding liquid, forming the antibubble. Finally Beilharz et al. [17] determined the conditions to form antibubbles by impacting a highly viscous droplet into a liquid bath of low viscosity. Remarkably, they obtained antibubbles with pure liquids, *i.e.* without the use of surfactants. However, in such a case, the lifetime of antibubbles they observed was of the order of 100 ms only.

By choosing appropriate surface-active molecules, the lifetime of an antibubble has been obtained to range from seconds to minutes [18]. The lifetime is the time needed for the air to drain in its shell by the action of gravity from the bottom, called South pole, to the top, called North pole, where it accumulates, forming an air pocket [19]. An antibubble dies when the thinning shell collapses near the South pole due to van der Waals interactions [18]. An antibubble is therefore an ephemeral object, despite the attempt to keep it alive for hours, *e.g.*, by shearing a confined antibubble in a spinning tube [2] or by Pickering stabilization of the interfaces with colloidal particles [14,20]. Understanding what governs the lifetime of antibubbles with surfactants alone remains therefore of prior importance.

Investigations during the last decade and a half have started on the instabilities at birth and death of antibubbles [9] and on the statistics of their lifetimes [18], followed by an empirical description of factors affecting their stability [21], controlling their formation [10] or influencing their bouncing [22], and ended by experimental [23] and theoretical [24] investigations on their collapse. In most of the experimental studies however, commercial detergents have been used to stabilize antibubbles, making it difficult to draw any conclusions on the mechanism responsible for their long lifetime, as detergent properties and exact compositions are usually not well documented.

Consequently, it has not been fully clarified yet to what extent a single surfactant molecule is suitable for generating antibubbles and which of its properties is responsible for maintaining long lifetimes. In an attempt to answer this question, Dorbolo et al. [25] have demonstrated the crucial influence of surface (visco-elastic) modulus on the antibubble lifetime, having used a mixture of three components [26], among which myristic acid, which confers to the interface very high surface viscosity of the order of 1 mPa.s.m. Subsequently, the role of surface viscosity to the antibubble lifetime has been rationalized theoretically by Scheid et al. [27] who showed the good agreement with experimental data. Their model, based on the lubrication theory for the air film drainage, relies on two main assumptions: (i) the adsorption characteristic time is much smaller than the antibubble lifetime such as surface-tension gradients induced by drainage are neutralized by rapid replenishing of surfactants on the interface; (ii) the surface dilatational viscosity is of the same order of magnitude than the surface shear viscosity, this latter being the only one that could be measured with a surface rheometer. Even though the first hypothesis is compatible with the surfactant mixture used in [25] for which adsorption timescale has been shown to span between 0.1 and 1 s [28], it is not compatible with other surfactants like $C_{12}E_6$, which have adsorption timescale of the order of hundred seconds [29], *i.e.* comparable to the antibubble lifetime using this surfactant [18]. Additionally, surface shear viscosity of small-molecule surfactants such as $C_{12}E_6$ is suggested to be extremely small, if not inviscid, as reported by Zell et al. [30]. Consequently, another effect than surface viscosity should be responsible for long lifetime of

the order of minutes. This effect is the surface elasticity, triggered when surface tension gradients occur as surfactants are transported away from the South pole during the drainage, provoking Marangoni stresses that opposes in turn to drainage.

The present paper investigates the role of surface elasticity in the lifetime of an antibubble, in addition to other effects such as the influence of the degree of saturation of the liquid with gas [31] and the influence of dust particles on the antibubble stability. Section 2 presents a general model which combines several aspects of models previously presented in literature, and shows numerical results demonstrating the crucial role of surface elasticity. Experimental settings are given in Section 3, along with a new antibubble generator [32] and independent surface elasticity measurements. Results and comparisons with the model are presented in Section 4 with sequential investigations of the influence of (i) surface elasticity, (ii) initial gas film thickness, (iii) liquid saturation with gas, (iv) dust particle size, (v) other surfactant and (vi) three-dimensional effects, on the antibubble lifetime. Conclusions are drawn in Section 5.

2. Theory

2.1. The model

We use in this section the lubrication model developed by Scheid [27] that includes the effect of surface shear viscosity η_s, and extended in [31] to account for gas dissolution into the surrounding liquid. Using the linear Boussinesq-Scriven surface fluid constitutive model [33], the model is further extended here to account for surface dilatational viscosity κ_s and surface elasticity E_s. Following Champougny et al. [34], exchanges of surfactants with the bulk are neglected in the dynamics but accounted for in the 'effective' elasticity E_s that can be measured independently in a Langmuir through for relevant interfacial velocities, and has been shown to depend on the bulk concentration above the critical micellar concentration (CMC). Since the Marangoni stress relies, *via* an equation of state written in the limit of insoluble surfactant, on the surfactant concentration at the interface Γ, a transport equation for surfactant is also needed [35]. But because the antibubble radius R remains constant during the antibubble lifetime, the variation of surfactant concentration induced by radial expansion can be neglected. The lubrication approximation is valid here because the initial film thickness h_0 is at least three orders of magnitude smaller than the radius. Therefore, only the lowest-order terms are considered in the asymptotical expansion with respect to the aspect ratio $\varepsilon = h_0/R \ll 1$. Details on the derivation and non-dimensionalisation of the resulting model are provided in Appendix B and only the final set of dimensionless evolution equations is given here, in which axisymmetry along the axis aligned with gravity g has been assumed:

$$\begin{aligned}
\frac{\partial h}{\partial t} &= -\frac{1}{\sin(\pi\theta)}\frac{\partial}{\partial\theta}\left[h\,\sin(\pi\theta)\left(u_s - \frac{h^2}{6}\frac{\partial p}{\partial\theta}\right)\right] - 2St(1-\beta)\left(1+\sqrt{\frac{\lambda}{\pi t}}\right),\\
\frac{\partial p}{\partial\theta} &= \frac{1}{2}\frac{\partial}{\partial\theta}\left[\cos(\pi\theta) - \frac{1}{\sin(\pi\theta)}\frac{\partial}{\partial\theta}\left(\sin(\pi\theta)\left[Bo\frac{\partial h}{\partial\theta} - 2\varepsilon\Theta Bq\;u_s\right]\right) + \frac{A}{h^3}\right],\\
h\frac{\partial p}{\partial\theta} &= (1+\Theta)Bq\left[\frac{\partial}{\partial\theta}\left(\frac{1}{\sin(\pi\theta)}\frac{\partial}{\partial\theta}(\sin(\pi\theta)\;u_s)\right)\right] + 2\pi^2 Bq\;u_s - \frac{Ma}{\Gamma}\frac{\partial\Gamma}{\partial\theta},\\
\frac{\partial\Gamma}{\partial t} &= -\frac{1}{\sin(\pi\theta)}\frac{\partial}{\partial\theta}\left[\sin(\pi\theta)\left(\Gamma\;u_s - \frac{1}{Pe_s}\frac{\partial\Gamma}{\partial\theta}\right)\right].
\end{aligned} \tag{1}$$

The polar coordinate θ has been scaled with π and spans from $\theta = 0$ at the South pole to $\theta = 1$ at the North pole of the antibubble. The time t has been scaled with $\tau_0 = \mu_g\pi^2 R/(\rho_\ell g h_0^2)$ corresponding to the viscous-gravity timescale for drainage between rigid interfaces and where μ_g is the gas viscosity and ρ_ℓ is the liquid density. The gas shell thickness $h(\theta,t)$, the surface velocity $u_s(\theta,t)$, the surface concentration $\Gamma(\theta,t)$ and the pressure in the shell $p(\theta,t)$ have been scaled, respectively, with h_0, $\pi R/\tau_0$, Γ_0 and $p_0 = 2\rho_\ell g R$; Γ_0 being the initial concentration of surfactant at time $t = 0$ and p_0 being the hydrostatic pressure difference driving the gas shell drainage. The parameter β measures the degree of saturation of the gas in the liquid: $\beta = 1$ corresponds to a fully saturated liquid, while $\beta = 0$ corresponds to a fully degassed liquid. The other dimensionless parameters are defined as follow:

$$\begin{aligned}
St &= \frac{\pi^2\mu_g D_\ell S_\ell}{\rho_\ell g h_0^3}, \quad \lambda = \frac{R^2}{\tau_0 D_\ell}, \quad Bo = \frac{\gamma_0 h_0}{\pi^2\rho_\ell g R^3}, \quad A = \frac{A'}{6\pi\rho_\ell g R h_0^3},\\
Bq &= \frac{\eta_s h_0}{\pi^2\mu_g R^2}, \quad \Theta = \frac{\kappa_s}{\eta_s}, \quad Ma = \frac{E_s}{\rho_\ell g R h_0}, \quad Pe_s = \frac{\rho_\ell g R h_0^2}{\mu_g D_s},
\end{aligned} \tag{2}$$

in which D_ℓ and S_ℓ are respectively the molecular diffusion coefficient and the solubility of the gas in the liquid, γ_0 is the equilibrium surface tension, A' is the Hamaker constant and D_s is the surface molecular diffusion of surfactant molecules. The Stanton number (St) compares the ga dissolution rate to the rate of drainage, the transient parameter (λ) compares the bulk diffusion timescale R^2/D_ℓ to the drainage timescale, the Bond number (Bo) compares the capillary pressure to the hydrostatic pressure, the Hamaker number (A) compares the disjoining pressure to the hydrostatic pressure, the Boussinesq number (Bq) compares the surface shear viscous stress to the bulk shear viscous stress in the gas shell, the ratio (Θ) compares the surface dilatational viscosity to the surface shear viscosity, the Marangoni number (Ma) compares the surface elasticity to the hydrostatic pressure force, and the surface Péclet number (Pe_s) compares the surface convection and the surface diffusion of surfactants.

To ensure symmetry with respect to the vertical axis, the set of Eq. (1) is solved with the following boundary conditions at the poles,

$$u_s = \frac{\partial h}{\partial\theta} = \frac{\partial p}{\partial\theta} = \frac{\partial\Gamma}{\partial\theta} = 0 \quad \text{at } \theta = \{0,1\}. \tag{3}$$

Finally, uniform initial conditions for the thickness and the surface concentration are imposed, namely

$$h = \Gamma = 1 \quad \text{in } t = 0. \tag{4}$$

The model was implemented in Comsol using the PDE mode and a direct solver. The temporal solver uses the implicit backward differentiation formula (BDF) method at order 3 [36]. The number of elements was 3000 in the domain $\theta = [0,1]$ in order to ensure convergence, with mesh refinement near $\theta = 0$ to capture the film destabilization due to the van der Waals interactions (see [27] for details). Mesh-independence on the solutions was verified.

Table 1
List of dimensional parameters used in the simulations and the associated dimensionless numbers. Note that τ_0 and p_0 are calculated parameters.

Dimensional	Value	Dimensionless	Value
R [mm]	7	λ	1690
h_0 [μm]	3	β	1
ρ_ℓ [kg/m^3]	997	St	2.77×10^{-2}
g [m/s^2]	9.81	Bo	2.72×10^{-6}
γ_0 [mN/m]	30	A	1.15×10^{-6}
E_s [mN/m]	0.1	Bq	3.35×10^{-4}
η_s [Pa.s.m]	10^{-6}	ε	4.29×10^{-4}
κ_s [Pa.s.m]	10^{-6}	Θ	1
μ_g [Pa.s]	1.85×10^{-5}	Ma	0.487
A' [J]	4×10^{-20}	Pe_s	33,307
D_s [m^2/s]	10^{-9}		
D_ℓ [m^2/s]	2×10^{-9}		
S_ℓ [vol/vol]	0.02		
τ_0 [s]	14.5		
p_0 [Pa]	137		

2.2. Parametric analysis

Given the large number of dimensionless parameters associated to the various physical effects included in this modeling, one should restrict the parametric analysis to practical situations, and investigate some deviations of interest, essentially relative to surface elasticity E_s, saturation parameter β and antibubble dimensions R and h_0. Therefore, in the following, and unless specified otherwise, the parameter values used for solving the model (1–4) are those given in Table 1. These parameters correspond to an antibubble with air for the gas phase and, for the liquid phase, a Triton-X-100 surfactant solution at 10 CMC, with the critical micellar concentration CMC = 0.02%w/v [43]. Triton-X-100, noted TX-100 hereafter, is non-ionic and has no measurable surface shear viscosity [30]. For the sake of simplicity η_s and κ_s have been fixed to 10^{-6} Pa.s.m., *i.e.* one order of magnitude below the limit of resolution of the double wall ring (DWR) surface shear rheometer (TA Instruments Discovery HR-3) [37], that has been used as a consistency check. Note that the model has been derived in the distinguished limit of a shear flow [38]. Consequently, exploring the limit of vanishing surface elasticity requires one to keep a residual surface viscous stress. Actually, the distinguished limit of an extensional flow cannot be attained by the present model as the extensional viscous stresses in the bulk are negligible ε^2-order terms (see for instance [39] for hybrid model).

Additionally, the value of the surface diffusion coefficient has been estimated to be $D_s = 10^{-9}$ m^2/s. The precise value has however no consequence on the numerical results as the surface Péclet number is already very high, namely $Pe_s \gg 1$, which indicates a surfactant transport at the interface entirely governed by convection. Therefore the surface diffusion plays physically no role but is convenient for a numerical perspective, like an artificial diffusion. More importantly, the air shell of an antibubble being a closed system, the second-order diffusion term allows to impose the symmetry boundary conditions for the surface concentration Γ at the two poles, as specified in (3).

2.3. Numerical results

As we are interested in the influence of the surface elasticity on the antibubble lifetime, Fig. 2 shows the time evolution of the minimum film thickness at the South pole for several values of the surface elasticity. For vanishing surface elasticity, $E_s = 0.0001$ mN/m, the drainage is fast and essentially governed by the residual surface viscous stresses as no difference is observed with zero surface elasticity. In the drainage phase, the thinning of the shell at the South pole is $h_{\min} \propto t^{-1.11}$ and depends on the magnitude of the surface viscosities, as was shown in [27], the fact that the exponent is close to unity being a coincidence. The shell then thins until reaching the critical thickness for rupture due to van der Waals instability. As the elasticity is increased, $E_s = 0.005$ mN/m, the Marangoni stress induced by the depletion of surfactants at the South pole of the antibubble counters the drainage before the film becomes thin enough to be destabilized by van der Waals interactions. Interestingly, the behaviour of the thickness *versus* time is non-monotonic, and the minimum thickness increases as the Marangoni flow refills the air shell at the South pole, until concentration gradients weaken and the shell finally collapses. At that moment, one can assume that the rupture is "instantaneous" as compared to the drainage time. The Marangoni effect is therefore found to drastically increase the lifetime of antibubbles above a surface elasticity between 0.005 and 0.007 mN/m. The transition is thus sharp enough to define a threshold at $Ma_{\text{th}} = 0.029 \pm 0.005$. Above this transition, the lifetime is two orders of magnitude larger and does not depend anymore on the surface elasticity. Indeed, the lifetimes for $E_s = 0.1$ and 1 mN/m are comparable. In this regime, the drainage behavior approaches the limiting case of a film draining between two rigid interfaces, *i.e.* with no-slip conditions. This limit can be derived by setting $u_s = 0$ in (1), together with $\beta = 1$, and solving for spatially-independent thickness, *i.e.* $h = h(t)$, in the vicinity of the South pole, *i.e.* $\theta \to 0$, which gives

$$h_{\min} = \frac{1}{\sqrt{1 + \frac{\pi}{3} t}} \quad . \tag{5}$$

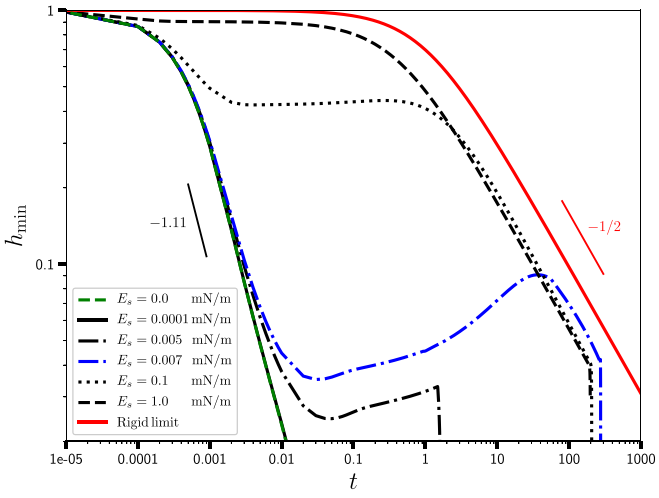

Fig. 2. Time evolution of the minimum shell thickness near the South pole for several surface elasticities corresponding to $Ma = \{0,0.0005,0.024,0.034,0.487,4.87\}$; see Table 1 for the other parameter values. The red line corresponds to the limiting case of an gas shell draining between two rigid interfaces, as described by Eq. (5). (For interpretation of the references to colour in this figure legend, the reader is referred to the web version of this article.)

The striking feature is that for sufficiently high surface elasticity, the antibubble lifetime can drastically increase due to Marangoni stresses. In order to illustrate this, Fig. 3 presents the profiles of h and u_s for three values of the surface elasticity taken at representative times as indicated by the colour scale. We observe that in the three cases, a gas pocket forms at the top of the antibubble as the gas accumulates due to drainage. However, the time at which this gas pocket is prominent depends on the surface elasticity. For low surface elasticity, $E_s = 0.0001$ mN/m, the surface velocity is always positive (see solid lines in (a) for u_s), the rupture occurs naturally at the South pole where the film is the thinnest and the lifetime is short. For an elasticity around the transition, $E_s = 0.005$ mN/m, the surface velocity changes sign in time between $t = 10^{-2}$ and 10^{-1} (see solid and dashed lines in (b) for u_s) indicating a Marangoni stress that opposes the drainage and refills the South pole for a while, *i.e.* with an increase of $h_{\min}$. For higher surface elasticity, $E_s = 1$ mN/m, the surface velocity changes sign in time and in space (see solid and dashed lines in (c) for u_s) for a much longer period, with a change of velocity sign (see the peak) that slowly travels toward the North pole.

Interestingly enough for $E_s = 0.005$ mN/m, the destabilization due to disjoining pressure occurs at the minimum thickness in the capillary ripple formed at the basis of the gas pocket, while for the other cases of Fig. 3, the destabilization of the film occurs at the vicinity of the South pole. The rupture location in turn can have an impact on the lifetime, and especially at the transition, as shown in Fig. 4 where the lifetime t_{life} (s), scaled with τ_0, is plotted *versus* the Marangoni number for different Bond numbers. The sharp transition in the lifetime at $Ma_{\text{th}}(\approx 0.03)$ presents a discontinuity corresponding to the jump in the rupture location: (i) at the South pole on the left of the discontinuity, as in Fig. 3a, and (ii) at the capillary ripple near the North pole on the right of the discontinuity, as in Fig. 3b; the capillary ripple triggering the van der Waals instability first. On the two plateau's before and beyond the transition, the rupture occurs essentially at the South pole as in Fig. 3a,c. Now, when decreasing the Bond number, hence the surface tension, the amplitude of the capillary ripple is less pronounced and the

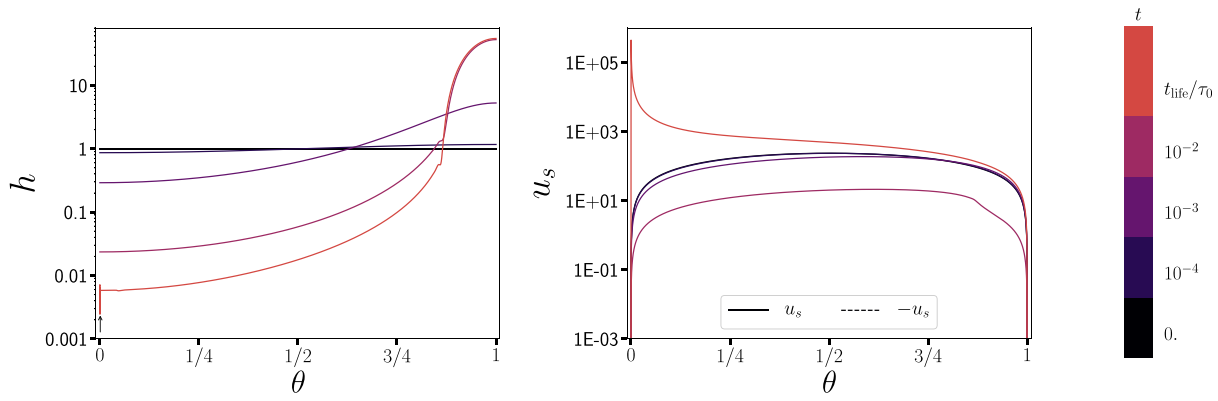

(a) $E_s = 0.0001\,\mathrm{mN/m}$

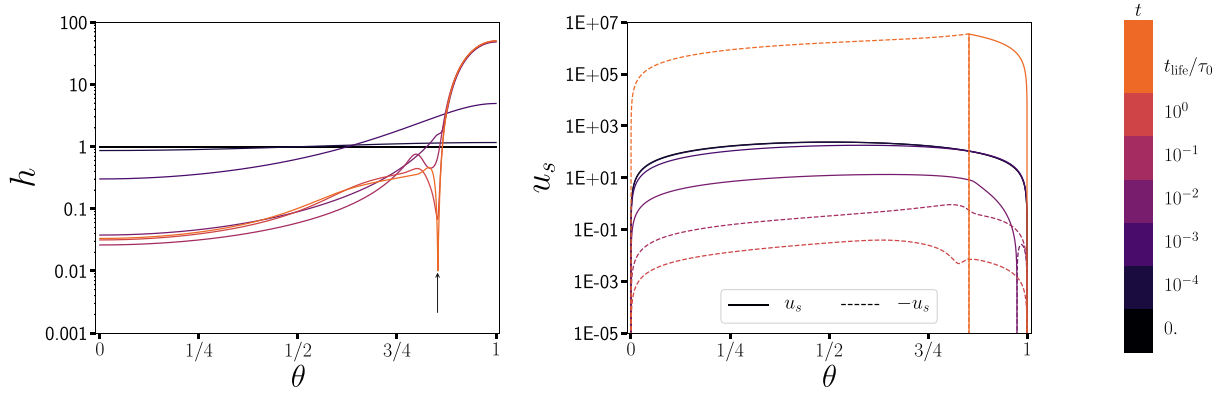

(b) $E_s = 0.005\,\mathrm{mN/m}$

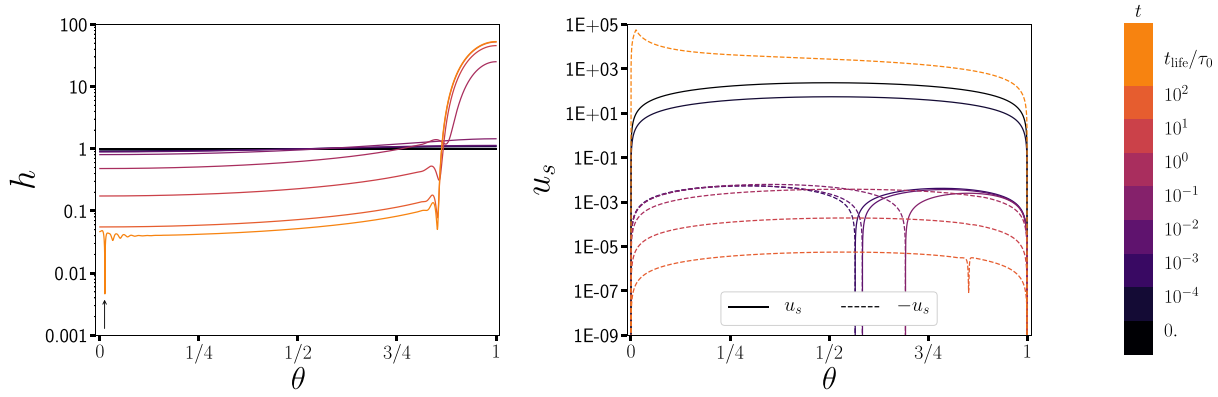

(c) $E_s = 1\,\mathrm{mN/m}$

Fig. 3. Time-evolution of the thickness and surface velocity profiles along the polar coordinate for three different elasticities corresponding to $Ma = \{0.0005, 0.024, 4.87\}$; see Table 1 for the other parameter values. The rupture position is near the South pole for (a) and (c) and at the capillary ripple near the North pole for (b). Arrows indicate the rupture location (see text for details). The colour code indicates the dimensionless time with t_{life}/τ_0 the last time of the simulation. (For interpretationof the references to colour in this figure legend, the reader is referred to the web version of this article)

rupture rather occurs essentially at the South pole. For $Bo = 9.1 \times 10^{-8}$ (blue line in Fig. 4), the discontinuity is even absent. Finally the lifetime increases with increasing surface tension, as capillary forces oppose to van der Waals interactions in the destabilization mechanism leading to rupture.

With the aim to compare the numerical results with experimental ones in Section 4, we plot in Fig. 5 the dimensional lifetime *versus* the radius of antibubbles for various surface elasticities. For sufficiently small antibubbles, surface elasticity can be strong enough to oppose to the drainage and delay drastically the lifetime. Now, for a given elasticity, there is always a radius beyond which the Marangoni effect is not strong enough to counteract the drainage, whose strength is proportional to the radius R measuring the hydrostatic pressure difference. The Marangoni number indeed compares the two effects. Nevertheless,

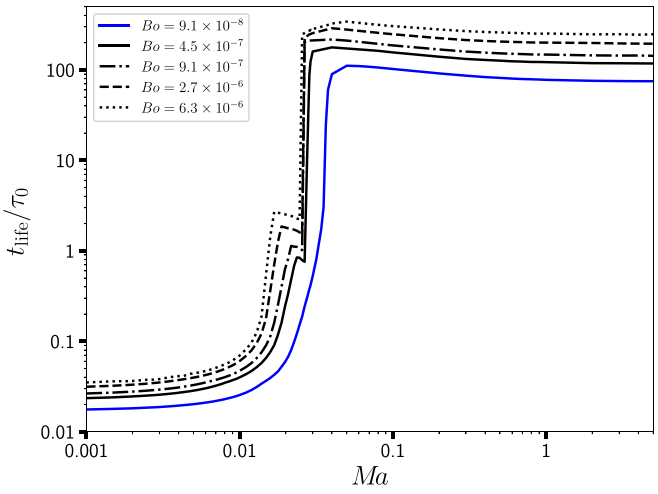

Fig. 4. Antibubble lifetime in function of the Marangoni number for several surface tension $\gamma_0 = \{1,5,10,30,70\}$ mN/m; see Table 1 for the other parameter values.

for sufficiently large surface elasticity, *i.e.* $E_s = 1$ mN/m, the Marangoni effect dominates the drainage over a wide range of antibubble radii. The Marangoni number does play a similar role here than the 'rigidity' parameter introduced in the context of film formation by Champougny et al. [34]. Above the transition value, the interfaces are rigidified by the Marangoni stress, while below this transition, there is a loss of rigidity that results in the impossibility of making long-living antibubbles, exactly like in the formation of soap films [34]. This loss of rigidity appears for $Ma_{th} \lesssim 0.03$, as was shown in Fig. 4. Note that the discontinuity in the curve for $E_s = 0.001$ mN/m in Fig. 5 is again due to a sudden change of rupture location. In other words, the change in interfacial mobility and motion is causing changes in the evolution of the thickness profile, leading, among other things, to a change in rupture location.

3. Experiments

The dependence of the antibubble lifetime on the radius found in Fig. 5 does not match the experimental observations reported in literature so far [18,21] showing no trend, possibly because of a wide dispersion of lifetimes as compiled in Table 2. Among the various potential sources of dispersion, there is the way antibubbles were made in

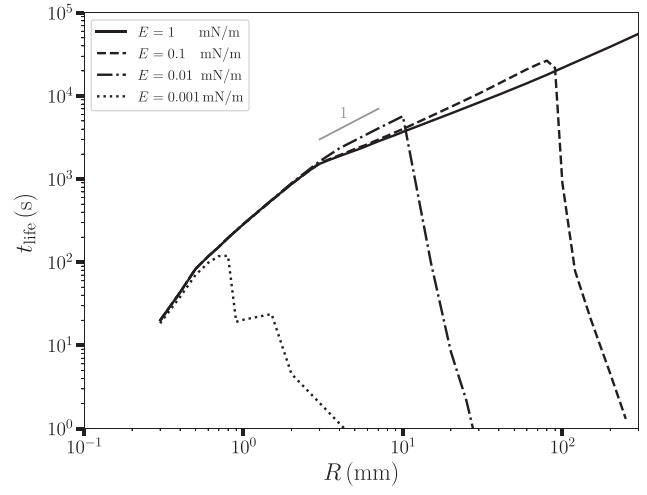

Fig. 5. Antibubble lifetime as a function of the radius for various surface elasticities; see Table 1 for the other parameter values. The slope '1' corresponds to the limit of rigid interfaces, *i.e.* $t_{life} \propto R$ as it can be deduced from Eq. (5), using the timescale τ_0.

Table 2
Range of antibubble lifetimes in literature experiments with no trend with the antibubble radius due to a wide dispersion of the data.

Surfactant	Radius (mm)	Lifetime (s)	Ref.
Dawn™ Ultra + NaCl	{3−11}	{5–60}	[21]
$C_{12}E_6$ at 10 CMC	{3–15}	{5–700}	[18]

previous studies, namely by hand, preventing their controlled production. We therefore designed an antibubble generator that allows to produce on-demand antibubbles in a reproductive manner and by controlling the gas phase. Next we briefly present the antibubble generator (see details in [32] and video in [40]), the materials and methods, the surfactant characterization, and liquid viscosity measurements.

3.1. Antibubble generator

The system shown in Fig. 6 consists of an immersed bell into a liquid bath, an injector tube, a pressure controller (Fluigent MFCS™-EZ) to deliver the fluids and two solenoid valves (Fluigent 2-SWITCH™) to dispense the liquid and gas on demand. The gas pressure is adjusted to maintain the position of the gas-liquid interface at the bottom of the bell. The liquid inlet produces a jet inside the bell through the injector. Fig. 7 shows the time sequence for producing antibubbles. At about 60 ms after the liquid injection, the jet penetrates the gas-liquid interface entraining a thin gas shell. This gas-wrapped jet destabilizes and pinches-off by the Rayleigh-Plateau instability [10] at around 180 ms. Once formed, it takes about 250 ms for the capillary oscillations to be damped and the antibubble to become spherical. The whole formation process takes less than half a second. Note the liquid injection needs to be interrupted using the valves before making the next antibubbles, such as to recreate a gas shell.

As compared to hand-made antibubbles [10], this set-up allows a much finer control of the various parameters influencing the formation, such as the diameter of the tip of the liquid injector, the distance

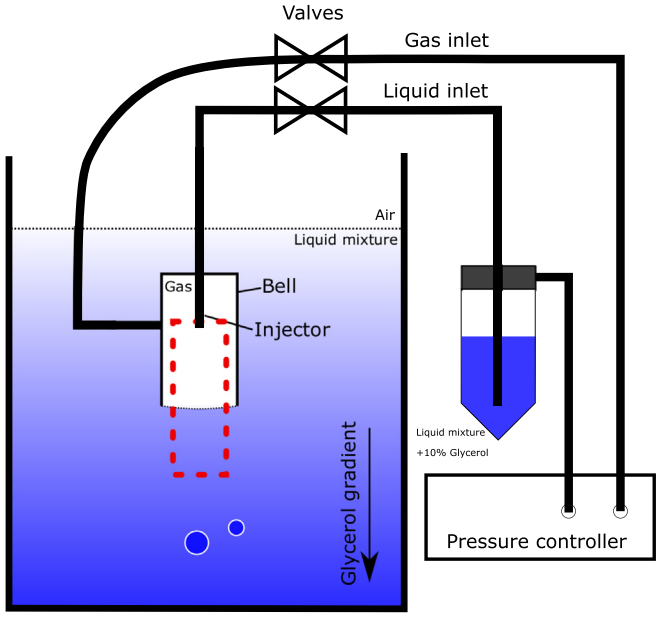

Fig. 6. On-demand antibubble generator. The tank size is $10 \times 10 \times 10$ cm^3, the bell's size is 4 cm in height and 1×1 cm^2 in cross section, the internal diameter (ID) of the injector is 0.7 mm and the distance between the injector and the interface is about 2 cm. The dashed red rectangle indicates the observation area for the time sequence of Fig. 7. (For interpretation of the references to colour in this figure legend, the reader is referred to the web version of this article.)

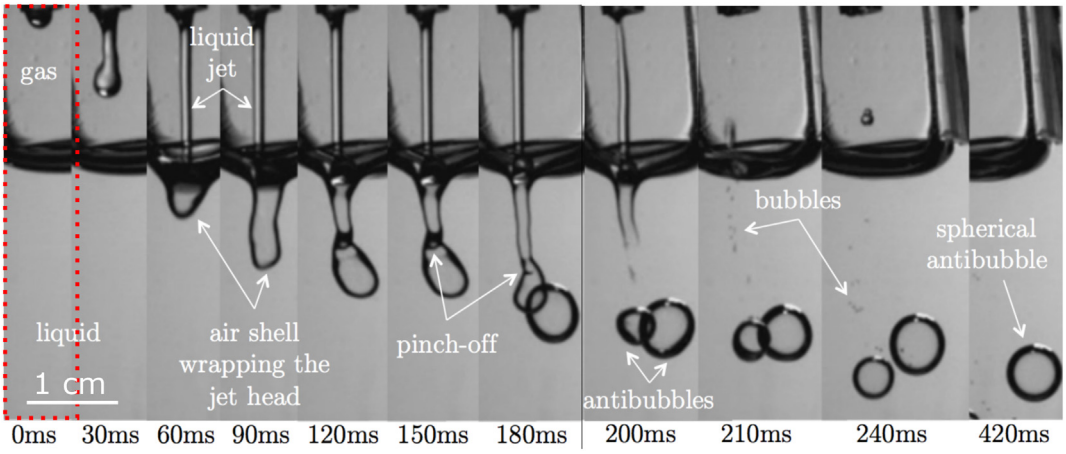

Fig. 7. Time sequence of antibubble formation (200 fps, 1 ms exposure time). Note that the width of each frame size is different. The dotted rectangle corresponding to the zone of interest, as schematized in Fig. 6, measures 0.8×4.6 cm^2.

between this tip and the gas-liquid interface, the velocity of the injected liquid jet and the nature of the gas. More specifically, two internal diameters (ID) of the injector were used in this study to increase the range of antibubble radius: (i) for ID = 0.7 mm, the range is $R = [0.5,2.5]$ mm, and (ii) for ID = 1.6 mm, the range is $R = [1,4]$ mm. The distance of the injector with the gas-liquid surface at the bottom of the gas bell was also adapted, namely (i) $d = 20$ mm, and (ii) $d = 25$ mm.

In order to minimize the influence of external perturbations on antibubbles, they were sank by adding 10%vol of glycerol to the surfactant mixture used to form the core. To prevent the antibubble to collapse when reaching the bottom of the tank, a gradient of glycerol was created inside the bath. Consequently, the antibubble sank until reaching the neutrally buoyant position located between two to four centimetres above the bottom, depending on their size and gas shell thickness. With a variation of less than 0.2%, the concomitant pressure, and hence solubility differences are small enough to have no significant influence on the antibubble lifetime.

3.2. Materials and methods

In the present study, Triton X-100 (TX-100) and $C_{12}E_6$ surfactants were used to produce antibubbles. TX-100 (purity ≥99%), $C_{12}E_6$ (purity ≥98%) and glycerol (purity ≥99%) were purchased from Sigma-Aldrich®. Surfactants were diluted in ultra-pure water obtained by an Arium UV PRO (Sartorius®) (conductivity ≤0.055 μS/cm). Filtered and oil-free compressed air purchased from Air Liquide was used to fill the bell of the antibubble generator and pressurize the liquid injector. Before each experiment the entire set-up was cleaned with Isopropyl alcohol and thoroughly rinsed with ultra-pure water. A Fibox 4 probe (Presens®) was used to measure the saturation of Oxygen in the bath assuming that the measurement of Oxygen saturation corresponds to air saturation in water in standard conditions [41]. The liquid was bubbled during several hours before each set of experiments. A saturation value between 96% and 98% with an accuracy of 2% was measured during experiments at the periphery of the reservoir such as the probe did not disturb the antibubble formation.

Antibubbles were observed using an Y3 high speed camera (IDT Vision®) with a pixel size of 10.85 μm and acquisition frequency of 30 Hz, which allow measuring accurately their sizes with a resolution of 80 μm on the diameter and their lifetimes with a resolution of 70 ms, taken from their generation to their collapse. All antibubble were observed from the bottom of the tank, except images on Fig. 7 taken form the side (see dashed red rectangle) and at a rate of 1000 Hz. All experiments were conducted in an ISO 7 clean room at a temperature of 20 °C, unless specified otherwise.

3.3. Surfactant characterization

In order to compare experimental data with the model, the surfactant mixture properties are required. Surface elasticity and density were measured for mixtures of TX-100 at 3, 5 and 10 CMC with and without glycerol. Elasticity of TX-100 was measured using a Langmuir trough (model KN 1003 from Biolin Scientific®) and following the protocol of Champougny et al. [34] consisting in measuring the time evolution of the surface tension $\gamma(t)$ while the barriers at the liquid interface are moved apart at constant speed V_b, starting with the equilibrium surface tension $\gamma_0 = \gamma(t = 0)$. Fig. 8 presents the elasticity of TX-100 for several barrier speeds. Similar to the results of [34] for $C_{12}E_6$, surface elasticity decreases with an increase of the bulk concentration of TX-100. We recall here that the surface elasticity is modelled as if the surfactant was insoluble, even though exchanges between the surface and the bulk are present. We thus believe that the decrease of this 'effective' surface elasticity is a consequence of the decrease in excess surface concentration. It is observed that the presence of glycerol does not affect the elasticity measurements at both concentrations of TX-100. Notice that for speeds corresponding to antibubble drainage dynamics, *i.e.* $V_b \leq 10^{-4}$ m/s, the surface elasticity is independent of V_b, as illustrated by the dashed lines, which allows us to use a mean value

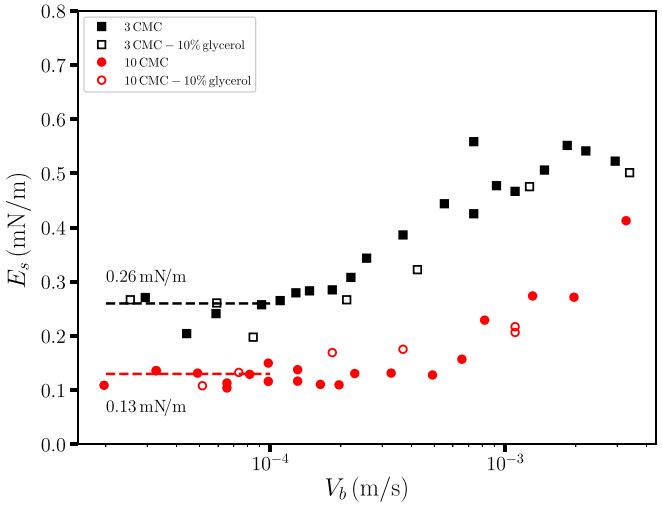

Fig. 8. Surface elasticity measurements using a Langmuir trough for various barrier speeds V_b. Increasing the concentration of TX-100 decreases the surface elasticity. The glycerol has no significant influence on the surface elasticity.

Table 3
Properties of surfactant mixtures at 25 °C used in antibubble experiments. Mixture with 10%vol of glycerol have similar values to those without glycerol except for density.

Mixture	γ_0 (mN/m)	E_s (mN/m)	ρ_ℓ (kg/m^3)
$C_{12}E_6$ 10 CMC	32.0 [42]	0.18 [34]	997 ± 2
TX-100 3 CMC	30 [43]	0.13	995 ± 2
TX-100 3 CMC with glycerol	30	0.13	1018 ± 2
TX-100 10 CMC	30 [43]	0.26	995 ± 2
TX-100 10 CMC with glycerol	30	0.26	1018 ± 2

for each concentrations of TX-100 used. Liquid densities are determined by measuring the weight of a given volume. These measurements are reported in Table 3.

Note that the measured surface elasticities are much smaller by at least two orders of magnitude than the Gibbs elasticity reported by Wantke et al. [44] for Triton-X-100. Nevertheless, these elasticities correspond to surfactant concentrations much below the CMC by at least one order of magnitude. They also have been obtained for strain rates much larger than 1 Hz. On the contrary, and similarly to Champougny et al. [34] for $C_{12}E_6$, the strain rates in our measurements are below 0.1 Hz and the surfactant concentrations are much above the CMC, which explains why the 'effective' elasticities are much below the values in [44], essentially because it is strongly affected and actually reduced by surfactant exchanges between the bulk and the interface.

3.4. Liquid viscosity

The bulk liquid viscosity of the TX-100 mixture without glycerol has been measured with a HAAKE™ Falling Ball Viscometer type C (Thermofisher scientific®), which lead to $\mu_\ell = 0.908$ mPa.s at 25 °C and for a 10 CMC concentration. Note that the liquid viscosity is only needed in Section 4.2 to estimate the initial film thickness from the rising velocity of antibubbles. Otherwise, the bulk liquid viscosity is not involved in the modeling since in the context of lubrication approximation, the viscous shear at the interfaces from the liquid phase is negligible as compared to the viscous shear from the gas phase, as long as $\mu_\ell/R \ll \mu_g/h_0$. This inequality is still verified with a 10% glycerol solution as the viscosity remains of the same order of magnitude, namely 1.21 mPa.s [45,46]. Therefore, the increase of viscosity due to the presence of glycerol in the liquid phase has been assumed in this work to have no impact on the antibubble lifetime.

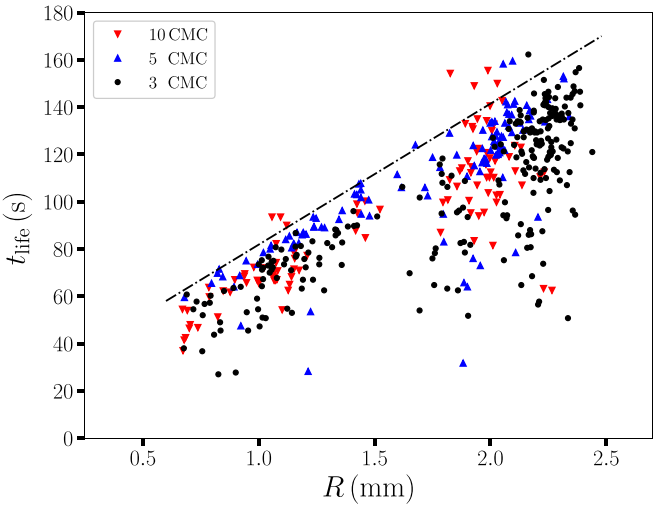

Fig. 9. Antibubble lifetime as a function of radius; mixture of water with TX-100 at 3, 5 and 10 CMC with 10%vol of glycerol. The dot-dashed line guides the eyes to emphasize the radius dependency of the lifetime.

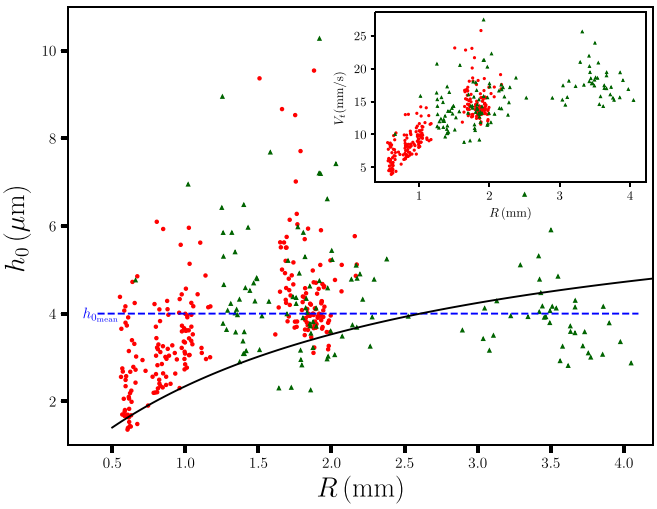

Fig. 10. Initial gas thickness obtained with Eq. (10) and using measurement of the terminal velocity V_t (see inset) for rising antibubbles in a mixture without glycerol and with TX-100 at concentration 10 CMC. Red disks and green triangles are data obtained with the 0.7 mm and 1.6 mm ID injector, respectively. The solid line is the theoretical prediction using an LLD model outlined in Appendix A. (For interpretation of the references to colour in this figure legend, the reader is referred to the web version of this article.)

4. Results

In this section, we aim at unravelling the wide dispersion of antibubble lifetimes observed experimentally by sequentially sounding the various possible sources of dispersion, in light with the theoretical model of Section 2.1.

4.1. Role of surface elasticity

The first set of experiments have been realized with a mixture of TX-100 at different concentrations to probe the influence of the surface elasticity on the antibubble's lifetime. Fig. 9 presents the lifetime for three concentrations and for radii ranging from 0.5 to 2.5 mm. During experiments, some antibubbles collapsed when they contact another antibubble or any solid part of the system. Those premature deaths

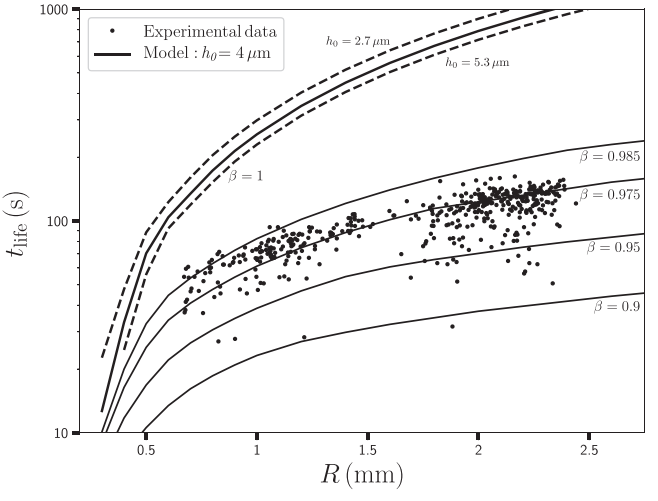

Fig. 11. Computed influence of initial gas thickness h_0 and saturation parameter β on antibubble lifetime with $E_s = 0.2$ mN/m and comparison with experimental data (black circles); see Table 1 for the other parameter values. Solid line represents simulations obtained with $h_0 = 4$ μm, while the dashed lines are obtained with $h_0 = 4 \pm 1.3$ μm, corresponding to the standard deviation of the thickness measurements presented in Fig. 10.

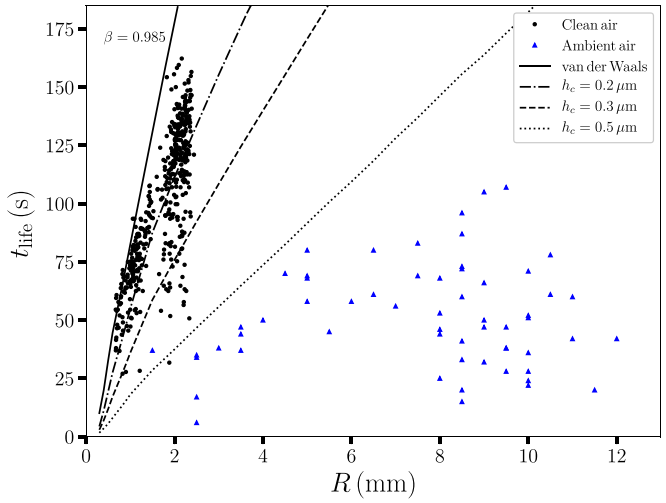

Fig. 12. Comparison of experimental lifetime with numerical simulations for several critical thicknesses h_c. For the numerical simulations, $E_s = 0.2$ mN/m, $h_0 = 4$ μm and $\beta = 0.985$; see Table 1 for the other parameter values. Experimental data come from two data set obtained with TX-100 mixture: a set obtained with the antibubble generator in an ISO 7 clean room (black circles), and a set obtained by hand in ambient air (blue triangles). (For interpretation of the references to colour in this figure legend, the reader is referred to the web version of this article.)

are not related to the drainage dynamic of the gas shell and have then been disregarded from the experimental data.

Firstly, Fig. 9 shows no significant influence of the concentration of surfactant on the antibubble lifetime. This is in accordance with the numerical results of Fig. 4 showing that, above a threshold value of the Marangoni number, the lifetime remains constant for a fixed equilibrium surface tension. Considering the surface elasticity reported in Table 3, and for the given range of radius, the Marangoni number is always larger than unity, *i.e.* much larger than $Ma_{th} \sim 0.03$ below which the interfaces loose their rigidity.

Secondly, experimental results demonstrate a clear dependence of antibubble's lifetime on the radius, a trend that has never been reported experimentally before, even though it is supported by classical drainage theory (see for instance [47]) and actually in agreement with our numerical results plotted in Fig. 5.

Despite the observation that the model captures the correct trend, the experimental results depict a large dispersion that prevents any quantitative comparison and therefore needs further inspection. Since the three concentrations investigated in Fig. 9 are not discriminating in terms of surface elasticity, the three corresponding sets of data are represented as a single set in the following and the mean value of surface elasticity extracted from Fig. 8, mainly $E_s = 0.2$ mN/m, is fixed hereafter for further comparison with the model.

4.2. Influence of initial gas thickness

Prior to any quantitative comparison with the model, one needs to evaluate the potential source of dispersion originating from the variation in the initial thickness of the gas shell. Actually, despite the automatic antibubble generation, the gas-liquid interface is continuously deformed by surface waves produced by previous generated antibubbles. Consequently, variability exists in the way the liquid jet impinges the gas liquid interface and entrains the gas, which can in turn influence the initial gas shell thickness. An estimation of this initial shell thickness can be obtained with the measurement of the terminal velocity of rising antibubbles [21], provided no glycerol is used. The terminal velocity results from the balance between the buoyancy force, due to the density difference of the antibubble compared to the surrounding liquid, and the drag force. By considering that $h_0/R \ll 1$, this balance writes

$$\frac{4}{3}\pi R^3(\rho_\ell - \rho_{AB})g = \frac{1}{2}\pi R^2 \rho_\ell C_D V_t^2, \tag{6}$$

where ρ_{AB} is the density of the antibubble, C_D is the drag coefficient and V_t is the terminal velocity of the rising antibubble. Neglecting the gas density as compared to the liquid density, the density difference can be approximated by

$$\rho_\ell - \rho_{AB} = \frac{3h_0}{R}\rho_\ell \ . \tag{7}$$

Combining Eqs. (6) and (7) yields an expression for the initial film thickness

$$h_0 = \frac{C_D V_t^2}{8g} \ . \tag{8}$$

Similarly to the study of Kim and Vogel [21], the antibubble is considered as a rigid sphere, which is supported by a large Marangoni number corresponding to high surface rigidity. This was also observed by Matsumoto et al. [48] who measured the terminal velocity of a bubble in a mixture with a small amount of Triton-X-100 ($c \ll$ CMC), and found drag coefficients coinciding perfectly with the one of a rigid sphere in the range $50 < Re < 90$. Here also, and contrarily to [21], we consider the corresponding drag coefficient in the intermediate range of Reynolds numbers, as encountered in our experiments, *i.e.* $5 < Re < 200$, with $Re = 2\rho_\ell V_t R/\mu_\ell$. According to Allen's drag model [49], an approximate drag coefficient for a rigid sphere in this range is

$$C_D \approx 18.5\, Re^{-3/5} \ , \tag{9}$$

which agrees within maximum 15% difference with the more accurate correlation of Turton and Levenspiel [50] as shown in [51]. Plugging

Table 4
Occurrence ratio of antibubbles with entrapped dust particles, depending on the antibubble radius R, particle size and environment. The volume of entrapped air is calculated as $4\pi R^2 h_0$, with $h_0 = 4$ μm. The data for ambient air are mean values taken from [55].

	Iso 7 clean room		Ambient air	
	≥0.5 μm	≥0.3 μm	>0.5 μm	≥0.3 μm
Nbr of particles/m^3	352,000	N.A.	~5×10^7	~2.5×10^8
$R = 2.5$ mm	1:9000		1:64	1:13
$R = 10$ mm	1:565		1:4	1:1

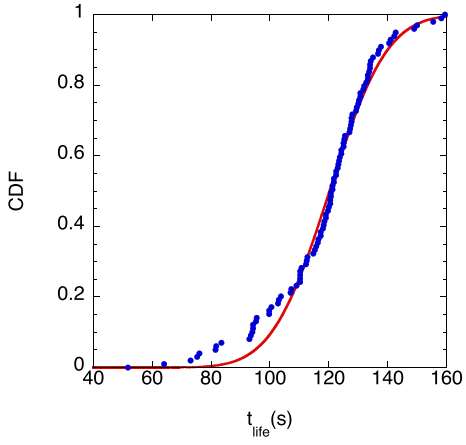

Fig. 13. Cumulative distribution function of the lifetimes of antibubbles having a radius between 1.9 and 2.1 mm (data extracted from Fig. 9). The solid curve corresponds to a fit using the CDF_G of the Gaussian distribution with the mean $\hat{t}_{life} = 120$ s and the variance $\sigma = 15.5$.

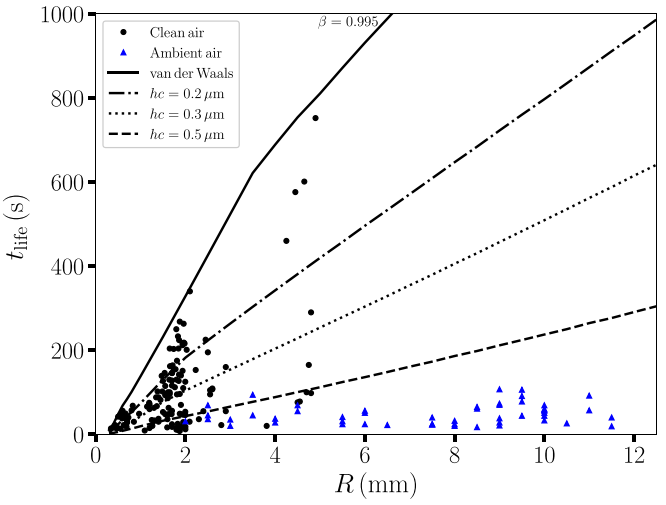

Fig. 14. Same as for Fig. 12 with $C_{12}E_6$ at 10 CMC and $\beta = 0.995$.

Eq. (9) into Eq. (8) finally gives

$$h_0 \approx \frac{1.526}{g}\sqrt[5]{\frac{\mu_\ell^3\ V_t^7}{R^3\ \rho_\ell^8}}\ . \tag{10}$$

Fig. 10 presents the measurements of h_0 obtained with Eq. (10) using the observable V_t, for 130 rising antibubbles with radii ranging between 0.5 and 4 mm. The mean initial gas shell thickness is $h_{0_{mean}} = 4\ \mu m$ with a standard deviation of ± 1.3 μm. The inset of Fig. 10 shows that for small antibubbles (red disks), the terminal velocity increases with R, while it is rather constant for larger antibubbles (green triangles). The explanation can be found in the formation mechanism of the antibubble, which relies on the Landau-Levich-Derjaguin law, as explained in Appendix A. As inferred from the set of Eqs. (A.1–8), if the radius a of the penetrating jet is smaller than the capillary length ℓ_c, h_0 strongly depends on R, otherwise it does only slightly depend on it. This is illustrated by the solid line in Fig. 10, showing a compatible trend with the data even though the dispersion remains important. This is mainly due to the variability of the velocity (U) of the impacting jet that can vary in a wide range, *i.e.* $0.1 < U < 0.4$ m/s, and has not been systematically measured. To a lower extent, the wavelength parameter (α) of the instability, can also vary and depends on the jet impact, as outlined in Appendix A. Few extreme values are also observed in Fig. 10, up to $h_0 = 10$ μm, which can be due to flow movements in the bulk liquid or to interactions with other antibubbles. Without clear causality, all points were taken into account in the normal distribution fitting the data. Now the mean value of 4 μm is in good agreement with values found in literature with other techniques, such as for instance $h_0 = 3.2$ μm using the gas dissolution time as an observable [31], or $h_0 = 5$ μm inferred from the volume of the air bubble formed after the antibubble collapse [19].

Next, the measured value of h_0 is used in the model to compare with our experimental data as reported in Fig. 11. We observe a large difference between the theoretical and experimental lifetimes that cannot be explained by the dispersion of the initial gas thickness (± 1.3 μm), as delimited by the dashed lines. Note in addition that a larger initial gas thickness leads to a lower antibubble's lifetime, which is counter-intuitive. It can be explained by the larger velocity of the gas in the shell during the early viscous drainage phase, *i.e.* before the Marangoni effect settles down and opposes to the drainage. As no significant influence of the initial gas shell thickness has been obtained, even in presence of large dispersion, we keep the value fixed to the mean value $h_0 = 4$ μm in the following and look for other effects.

4.3. Influence of gas saturation

A possible explanation for the lower antibubble's lifetime observed experimentally is the undersaturation of the bulk liquid with gases that leads to the partial dissolution of antibubble gas shell [31]. Indeed, despite the special care we took in having a bulk saturated in gas, we measured slightly under-saturated values, *i.e.* $\beta < 1$, with our oxygen probe, even though by only few percents. Yet, we compare in Fig. 11 the experimental lifetimes with numerical predictions computed for different gas saturation parameters β.

The model predicts a significant decrease of the lifetime for only few percents of undersaturation, hence in the limit of resolution of the oxygen probe. These results demonstrate the importance of controlling the gas content in the liquid when making antibubbles, as already reported in [31]. A key point here is that despite the uncertainty on the absolute value of the gas saturation, it was found to be very stable in time, within 2%. However, to encompass the shortest lifetime, one would had to set $\beta = 0.9$, which is much below the minimum value of saturation measured experimentally, namely $\beta = 0.97 \pm 0.02$. Consequently, even though quantitative agreement can finally be obtained with most of the experimental data when accounting for partial gas dissolution, it still does not explain the wide dispersion of the antibubble lifetime, and especially for the shortest lifetimes.

In what follows, we fix the saturation parameter to the upper bound in Fig. 11, *i.e.* $\beta = 0.985$, and focus on the rupture mechanism.

4.4. Influence of dust particles

The model assumes that the gas shell is destabilized by thermal fluctuations and van der Waals interactions when the average film thickness becomes smaller than about 100 nm [52]. What if instead the film prematurely breaks because of the presence of dust particles in the gas phase? This mechanism has been detailed by Denkov et al. [53] who analyzed the role of dust particles as antifoam "compounds". Evangelio-Sànchez [54] has recently demonstrated the crucial role of dust particles in the premature collapse of floating bubbles. We account for this phenomenon into the model by imposing an arbitrary critical thickness h_c at which an antibubble collapses. Fig. 12 presents the theoretical lifetime for three different critical thicknesses $h_c = 0.2$, 0.3 and 0.5 μm, in addition to the lifetime obtained with the van der Waals instability. As observed, increasing the critical rupture thickness by only few hundreds of nanometers affects significantly the lifetime of antibubbles. Moreover, to reproduce all the data (circles) obtained in a clean environment with our antibubble generator, one has to consider a critical thickness of 0.5 μm at most. This value is consistent with the fact that experiments where conducted in an ISO 7 cleanroom where only particles of diameter larger than 0.3 μm are filtered. Assuming long-range intermolecular forces of about 100 nm are finally responsible for the rupture, a particle of 0.3 μm might reasonably destabilize a shell of 0.5 μm thickness.

With the aim to better understand this rupture mechanism, we compare in Fig. 12 the lifetime of antibubbles produced in a clean environment to antibubbles produced in ambient air by hand, following the same procedure than in [18]. Without excluding a possible contribution of gas dissolution (see previous section), it is shown that antibubbles produced in ambient air have a smaller lifetime than those produced in a clean environment. These results confirm the strong influence of dust particles on antibubble lifetime, as they are more numerous and larger in ambient air than in a clean room. Actually, Table 4 shows the occurrence ratio for an antibubble to contain entrapped dust particles in the air shell for both environments.

Note on the one hand that the number of particles of size lower than 0.5 μm in an ISO 7 clean room is not available but the gas used with our antibubble generator came from a filtered air compressor. On the other hand, the occurrence ratio reported in Table 4 for airborne particles is only a rough estimate as it corresponds to outdoor measurements

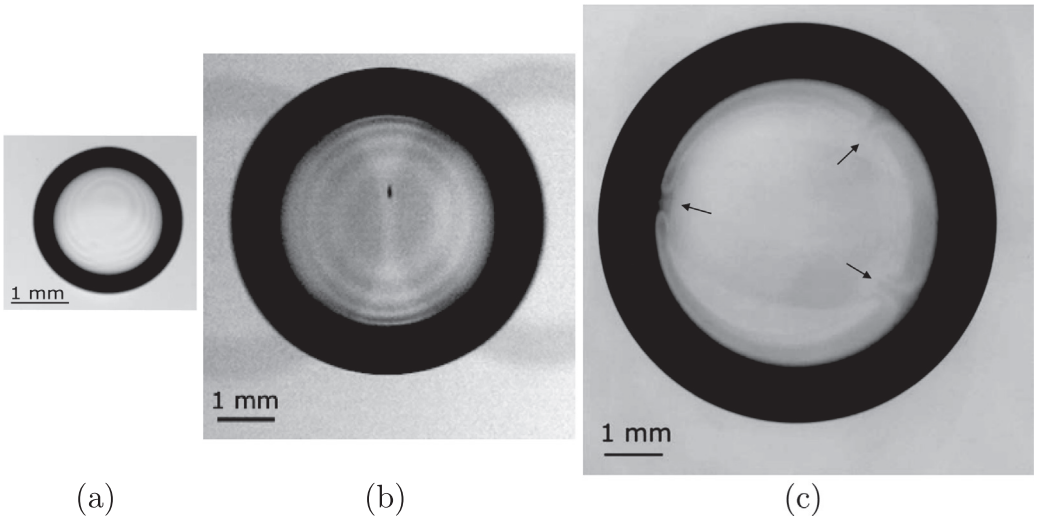

Fig. 15. Pictures of antibubbles illuminated by a monochromatic light: (a) antibubble made by our generator in the clean room using TX-100 and observed from the side; it shows regular interference fringes indicating a uniform drainage, (b) antibubble made by hand in ambient air using TX-100 and observed from the bottom; it shows concentric interference fringes, (c) same as (b) but using commercial detergent (Dreft); it shows non-regular interferences fringes, as pointed out by the arrows, indicating a non-uniform drainage. Each picture have the same scale.

made by [55], assuming that a correlation exists with indoor airborne particle concentration, as reported in [56]. Nevertheless, the occurrence ratio of dust-loaded antibubble is extremely low in a clean room, while it is much higher in ambient air, and especially for larger antibubbles, for which every antibubble of 10 mm radius should contain at least one particle of 0.3 μm. These data perfectly corroborate the observations reported in Fig. 12 for antibubble lifetimes.

To validate the influence of dust particles as the main cause for the antibubble collapse, we can consider the cumulative distribution function (CDF) of the lifetimes, which can naturally be described by the two-parameter Weibull distribution of the form:

$$\mathrm{CDF_W} = 1 - \exp^{-\left(\frac{t_{\mathrm{life}}}{t_0}\right)^k}, \tag{11}$$

where k and t_0 are the shape and the scale parameters, respectively. In previous works [18,25,31], the distribution of the antibubble lifetimes was found to follow a Markovian distribution, *i.e.* with $k = 1$. This implies that the collapse probability remained constant during the whole lifetime of the antibubble. The antibubbles in those earlier studies were made by hand without any control on the radius, the amount of dust particles and the gas content in the liquid phase. In Fig. 13, we report the CDF of the lifetimes for the antibubbles produced in controlled conditions using our antibubble generator and select the antibubbles having a radius between 1.9 and 2.1 mm only, as extracted from the data of Fig. 9. The red curve corresponds to the CDF of a Gaussian, namely

$$\mathrm{CDF_G} = \frac{1}{2}\left[1 + \mathrm{erf}\left(\frac{t_{\mathrm{life}} - \hat{t}_{\mathrm{life}}}{\sigma\sqrt{2}}\right)\right], \tag{12}$$

where $\hat{t}_{\mathrm{life}}$ is the average lifetime and σ the standard deviation. Remarkably, the best fit with a Gaussian distribution indicates that the antibubble collapse results from a deterministic process rather than a stochastic process, as it should inherently be the case for coalescence when dominated by thermal fluctuations [57]. This was confirmed by fitting the data using $\mathrm{CDF_W}$ (not shown) that gave a shape factor $k = 9.1$ and a scale factor $t_0 = 126$ s. Such a high shape factor in particular suggested a better fitting by a normal distribution. Consequently, the deterministic character of the film collapse that we have found confirms the dominant role of dust particles in determining the antibubble lifetime. And this has been straightforwardly accounted for in the modeling by imposing a critical thickness for rupture associated to the maximum size of the filtered particles.

4.5. Other surfactants

In order to complete the study, we have performed additional experiments with another surfactant, namely $C_{12}E_6$. Like TX-100, it is a non-ionic surfactant with a long adsorption timescale of about 100 s [29,43], *i.e.* comparable to the lifetime of antibubbles. This feature is crucial for the Marangoni effect to be important and for the validity of the model that relies on the insoluble limit [34].

For this mixture, we have improved the precision on the bulk saturation to $\beta = 0.995 \pm 0.005$ by adding a temperature control, and as for the measurements of the initial thickness h_0, two sizes of injector have been used to widen the range of antibubble radii to approximately one decade, *i.e.* from 0.5 to 5 mm. The surface elasticity value is left to $E_s = 0.2$ mN/m [34], since the results are not sensitive to variation of E_s above the "rigidity" threshold, *i.e.* for $Ma \gg 0.03$, which is also guaranteed here.

Results are plotted in Fig. 14. As predicted by our theory, antibubbles with $R = 5$ mm can live about 10 times longer than in ambiant air, *i.e.* about ten minutes instead of one, when made in a clean room with our antibubble generator and with a liquid almost saturated in gas. As for TX-100, the smaller lifetime for antibubbles made by hand is probably due to both larger particles in the atmosphere and uncontrolled saturation of the liquid with gas.

These results with another surfactant confirms that controlling the liquid saturation is crucial to allow quantitative comparison between experiments and theory. And that the dispersion of data is most probably due to the presence of dust particles in the atmosphere.

4.6. Three-dimensional effects

Yet, a last source of the lifetime dispersion that we can think of is the three-dimensional effect that can lead to azimuthal destabilization of the gas shell. Some channeling has actually been reported in antibubbles [18,19], the mechanism of which has not been identified yet, even though the large observed wavelength suggests that it takes its origin in a hydrodynamic instability rather than being caused by

van der Waals interactions. One can be tempted to state that such channeling would shorten the lifetime in a significant manner, as most of the gas drainage would take place in the thicker channels, which are less hydrodynamically resistive than the thin shell elsewhere. Nevertheless, and as it can be observed in a video [58], the lifetime can instead be increased by three-dimensional instabilities reminiscent of the marginal regeneration encountered in soap films [59]. Indeed, as rationalized by Bruinsma [60] for soap films, patches of thicker air film could rise and induce gravity-driven convection into the air shell, sustaining the antibubble for a longer time.

In order to evaluate if these three-dimensional effects were present in our experiments, we have visualized antibubbles using monochromatic light. Fig. 15 shows three pictures of antibubbles taken from the side (a) and from the bottom (b-c). Black fringes can be seen and arise from interferences between the light being reflected on both interfaces of the air shell. All antibubbles obtained with TX-100 that we have checked showed uniform fringes as in Fig.15a-b, which suggests that no 3D effect can be responsible for the premature deaths of antibubbles observed in our experiments. Actually, we were not able to observe 3D effects, unless using commercial detergent, as shown in Fig. 15c with Dreft. In fact, the only picture in literature showing 3D effects can be found in [18] (Fig. 3), for which commercial detergent (Palmolive) was also used, even though not explicitly mentioned in that reference. Worth to mention is that the 3D effects observed in Fig. 15c were observed after some delay of about 100 s and did not immediately lead to rupture, suggesting as mentioned above a stabilizing mechanism similar to the marginal regeneration. Provided the lifetimes of hand-made antibubbles plotted in Fig. 12 and Fig. 14 (triangles) were all shorter than 100 s, one can state with confidence that the dispersion observed on the lifetimes are effectively due to dust particles, as explained in Section 4.4, rather than to 3D effects.

Note finally that our theoretical model relies on the axisymmetry of the antibubble and that the good agreement with experimental data, at least for the longest living antibubble, supports the argument that antibubbles generated in this work were indeed axisymmetric, as illustrated by the concentric interference fringes in Fig. 15b.

5. Conclusions

This work clarified the factors influencing the lifetime of antibubbles generated and stabilized with nonionic and small surfactant molecules that have a sufficiently slow surface adsorption time for the Marangoni stress to be present. By sequentially investigating all the possible effects using our on-demand antibubble generator, we have de-correlated each contribution, leading to the following findings:

(i) The lifetime of an antibubble is not controlled by surface viscosity for small surfactant molecules, however using an inviscid interface in the modeling did not yield representative results;
(ii) Surface elasticity represents the main mechanism to increase the lifetime of antibubbles, provided the Marangoni number, characterizing the surface rigidity, is larger than a threshold value $Ma_{\mathrm{th}} \approx 0.03$;
(iii) Above this threshold, the lifetime is shown to be almost independent on the surface elasticity, hence on the bulk concentration of the surfactant mixture;
(iv) Avoiding interference from gas dissolution and dust particles, antibubble lifetime is proven to increase with the antibubble radius;
(v) The initial shell thickness of the antibubble (of about 4 μm) has no crucial influence on the lifetime and does actually not depend significantly on the antibubble radius;
(vi) Accounting for gas dissolution in the liquid, even if it is as close as 0.5% of the saturation, is crucial to obtain qualitative agreement with modeling;
(vii) Even though the deterministic parts of coalescence is often difficult to identify, as pointed out in the recent review by Kamp et al. [61], our careful experiments allowed with confidence to attribute it to the presence of dust particles whose maximum size was bounded by filtration in both the clean room and the injected antibubble gas phase. On the contrary unfiltered dust particles that are also more numerous in the atmosphere provoke a higher occurrence of premature antibubble collapses, elucidating the mechanism conferring the stochastic character of the antibubble lifetime distributions observed previously in literature;
(viii) The occurrence ratio of dust-induced antibubble collapse is higher for large antibubbles than for small ones, as the volume of embedded gas scales with the square of the antibubble radius.
(ix) Three-dimensional flow effects were never observed in antibubbles made with TX-100, in the case of which comparisons with axisymmetric modeling should be valid.
(x) As long as 3D effects are concerned, there is a fundamental difference between pure surfactant mixtures used in this work and commercial detergents, which deserves further investigations.

Based on these findings obtained with Triton-X-100 mixtures, we have performed lifetime measurements with $C_{12}E_6$ in highly saturated liquids, and have shown that the lifetime of antibubbles can be increased by a factor ten, if obtained in a clean room environment, as compared to those obtained in ambient air. It is thus demonstrated through the present study that optimizing the lifetime of antibubbles is feasible, paving the way toward future applications requiring controlling the lifetime, like for instance in drug vectorization or all-aqueous emulsification.

Acknowledgements

We thank Joe Samaniuk for his assistance in measuring surface elasticities. We are also grateful to Nikolai Denkov and Dominique Langevin for fruitful discussions about three-dimensional drainage. We thank the IAP 7/38 MicroMAST project supported by BELSPO for financial support. S.D. and B.S. thank the F.R.S-FNRS for the financial support.

Appendix A. Origin of the initial shell thickness in an antibubble

This appendix aims at estimating the initial film thickness of the antibubble's air shell and capture a possible dependence with the antibubble radius. As shown in Fig. 7, the antibubble formation consists in a jet that penetrates into a liquid bath, entraining an annular film of air and pinching-off by the Rayleigh-Plateau instability [10]. This sequence is sketched in Fig. A.16, along with the relevant parameters. Note that the gas is considered to be air in this example. Following [62], who assumed the jet to behave like a solid cylinder moving at constant speed U, the thickness of the entrained air film can be evaluated by the Landau-Levich-Derjaguin law, namely

$$h_{\mathrm{LLD}} = \frac{1.34}{C} 4^{2/3} Ca^{2/3} \quad , \tag{A.1}$$

where C is a curvature factor driving the capillary suction in the air film, and $Ca = \mu_g U/\gamma_0$ is the capillary number. We used the factor $4^{2/3}$ instead of $2^{2/3}$ as in [62] to account for the surfactant-induced rigidity of the outer interface, contributing to the maximum thickening of the air film [34]. In the case of the jet radius a much larger than the capillary length $\ell_c = \sqrt{\gamma/(\rho_\ell g)}$, namely $a \gg \ell_c$, the capillary pressure driving the suction at the static meniscus is $\gamma_0\sqrt{2}/\ell_c$, like for flat films in perfectly wetting conditions [63]. In the opposite case, namely $a \ll \ell_c$, the driving capillary pressure is essentially γ/a [64]. Therefore, in the intermediate case for which $a \sim \ell_c$, the driving

capillary pressure is the addition of the two contributions, which thus lead to the following curvature factor

$$C = \left(\frac{\sqrt{2}}{\ell_c} + \frac{1}{a}\right) . \tag{A.2}$$

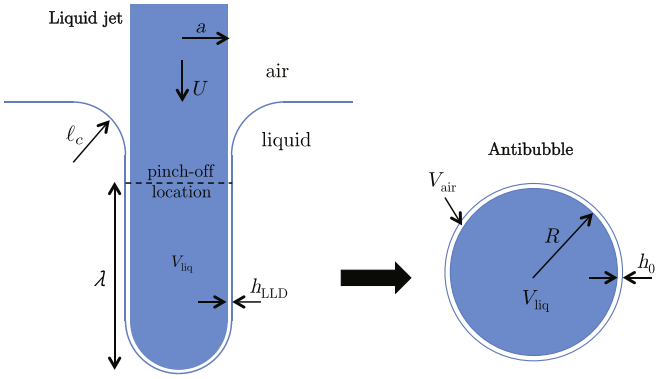

Fig. A.16. Sketch of the antibubble formation.

Based on linear stability theory, let us parametrise the length of the jet segment that will destabilize to form an antibubble by $\lambda = \alpha\ a$, where α characterizes the way the Rayleigh-Plateau instability is triggered. For a jet destabilising into the air, the most amplified mode corresponds to $\alpha = 9.01$ [65], but the cut-off wavelength is for $\alpha = 6.28$. Provided the jet instability is strongly influenced by the presence of the outer liquid, inducing in turn finite amplitude perturbations at the impact, we will consider in the following that α can take any value in the interval [6.28,9.01].

Matching the liquid volume V_{liq} of the destabilized jet segment, $\pi a^2\lambda$, with the liquid volume embedded in the antibubble, $4\pi R^3/3$, provided $h_0/R \ll 1$, yields

$$R = \sqrt[3]{\frac{3\alpha}{4}}\ a\ , \tag{A.3}$$

which shows that the antibubble size is essentially proportional to the jet radius. Matching now the volume V_{air} of the entrained air film, $2\pi a\lambda h_{LLD}$, with the air volume of the antibubble, $4\pi R^2 h_0$, and using (A.3), yield.

$$h_0 = \sqrt[3]{\frac{2\alpha}{9}}\ h_{LLD}\ . \tag{A.4}$$

Incorporating (A.1) and (A.2) into (A.3), while eliminating a using (A.3) finally gives a relationship between the initial film thickness and the antibubble radius. Taking $U = 0.1$ m/s and $\alpha = 6.28$ give the solid curve plotted in Fig. 10, using for the other parameters their values from Table 1.

Appendix B. Supplementary data: Model derivation

Supplementary data to this article can be found online at https://doi.org/10.1016/j.cis.2019.05.007.

References

[1] Hughes W, Hughes AR. Liquid drops on the same liquid surface. Nature 1932;129:59.
[2] Stong CL. The amateur scientist. Sci Am 1974;230(4):116–22.
[3] Iida Y, Takashima T. Direct-contact heat transfer characteristics: evaporation of a drop dropped onto a hot liquid surface. Int J Heat Mass Transfer 1980;23(9):1263–71.
[4] Nosoko T, Mori Y. Vaporization of drops of a denser, volatile liquid dropped onto a surface of another liquid. Trans ASME 1985;107:384–91.
[5] Johansen K, Kotopoulis S, Postema M. Ultrasonically driven antibubbles encapsulated by newtonian fluids for active leakage detection. Proceedings of the international multiconference of engineers and computer scientists, vol II; 2015. p. 1–5.
[6] Kotopoulis S, Johansen K, Gilja O, Poortinga A, Postema M. Acoustically active antibubbles. Acta Phys Pol A 2015;127(1):99–102.
[7] Postema M, Novell A, Sennoga C, Poortinga AT, Bouakaz A. Harmonic response from microscopic antibubbles. Appl Acoust 2018;137:148–50.
[8] Silpe JE, McGrail DW. Magnetic antibubbles: formation and control of magnetic macroemulsions for fluid transport applications. J Appl Phys 2013;113(17):17B304.
[9] Dorbolo S, Caps H, Vandewalle N. Fluid instabilities in the birth and death of antibubbles. New J Phys 2003;5(1):161.
[10] Kim PG, Stone HA. Dynamics of the formation of antibubbles. Europhys Lett 2008;83:54001.
[11] Tufaile A, Sartorelli JC. Bubble and spherical air shell formation dynamics. Phys Rev E 2002;66:056204.
[12] Postema M, ten Cate F, Schmitz G, de Jong N, van Wamel A. Generation of a droplet inside a microbubble with the aid of an ultrasound contrast agent: first result. Lett Drug Des Discov 2007;4(1):74–7.
[13] Poortinga AT. Micron-sized antibubbles with tunable stability. Colloids Surf A Physicochem Eng Asp 2013;419:15–20.
[14] Silpe JE, Nunes JK, Poortinga AT, Stone HA. Generation of antibubbles from core-shell double emulsion templates produced by microfluidics. Langmuir 2013;29:8782–7.
[15] Shen Y, Hu L, Chen W, Xie H, Fu X. Drop encapsulated in bubble: a new encapsulation structure. Phys Rev Lett 2018;120:054503.
[16] Bai L, Xu W, Wu P, Lin W, Li C, Xu D. Formation of antibubbles and multilayer antibubbles. Colloids Surf A Physicochem Eng Asp 2016;509:334–40.
[17] Beilharz D, Guyon A, Li E, Thoraval M, Thoroddsen S. Antibubbles and fine cylindrical sheets of air. J Fluid Mech 2015;779:87.
[18] Dorbolo S, Reyssat E, Vandewalle N, Quéré D. Aging of an antibubble. EPL (Europhys Lett) 2005;69(6):966.
[19] Suhr W. Gaining insight into antibubbles via frustrated total internal reflection. Eur J Phys 2012;33(2):443.
[20] Poortinga AT. Long-lived antibubbles: stable antibubbles through Pickering stabilization. Langmuir 2011;27(6):2138–41.
[21] Kim PG, Vogel J. Antibubbles: factor that affects their stability. Coll Surf A 2006;289:237–44.
[22] Zou J, Wang W, Ji C. Bouncing antibubbles. Exp Fluids 2016;57(9):147.
[23] Zou J, Ji C, Yuan B, Ruan X, Fu X. Collapse of an antibubble. Phys Rev E 2013;87(6):061002.
[24] Sob'yanin DN. Theory of the antibubble collapse. Phys Rev Lett 2015;114(10):104501.
[25] Dorbolo S, Terwagne D, Delhalle R, Dujardin J, Huet N, Vandewalle N, et al. Antibubble lifetime: influence of the bulk viscosity and of the surface modulus of the mixture. Colloids Surf A Physicochem Eng Asp 2010;365:43–5.
[26] Golemanov K, Denkov ND, Tcholakova S, Vethamuthu M, Lips A. Surfactant mixtures for control of bubble surface mobility in foam studies. Langmuir 2008;24:9956.
[27] Scheid B, Dorbolo S, Arriaga LR, Rio E. Antibubble dynamics: the drainage of an air film with viscous interfaces. Phys Rev Lett 2012;109:264502.
[28] Emile J, Salonen A, Dollet B, Saint-Jalmes A. A systematic and quantitative study of the link between foam slipping and interfacial viscoelasticity. Langmuir 2009;25:13412–8.
[29] Lin S-Y, Lee Y-C, Shao M-J. Adsorption kinetics of $C_{12}E_6$ at the air-water interface. J Chin Inst Chem Engrs 2002;33:631.
[30] Zell ZA, Nowbahar A, Mansard M, Leal LG, Deshmukh SS, Mecca JM, et al. Surface shear inviscidity of soluble surfactants. Proc Nat Am Soc 2014;111(10):3677–82.
[31] Scheid B, Zawala J, Dorbolo S. Gas dissolution in antibubble dynamics. Soft Matter 2014;10:7096–102.
[32] Anti-bubble generator. URL https://data.epo.org/publication-server/rest/v1.0/publication-dates/20170809/patents/EP3202491NWA1/document.pdf; Jun. 2017.
[33] Slattery JC, Sagis L, Oh E-S. Interfacial transport phenomena. 2nd ed. Springer Verlag; 2007.
[34] Champougny L, Scheid B, Restagno F, Vermant J, Rio E. Surfactant-induced rigidity of interfaces: a unified approach to free and dip-coated films. Soft Matter 2015;11(14):2758–70.
[35] Stone HA. A simple derivation of the time-dependent convective-diffusion equation for surfactant transport along a deforming interface. Phys Fluids A 1990;2(1):111–2.
[36] Curtiss CF, Hirschfelder JO. Integration of stiff equations. Proc Natl Acad Sci 1952;38(3):235–43.
[37] Vandebril S, Franck A, Fuller G, P M, Vermant J. A double wall-ring geometry for interfacial shear rheometry. Rheol Acta 2010;49:131–44.
[38] Breward CJW, Howell PD. The drainage of a foam lamella. J Fluid Mech 2002;458:379?406.
[39] Schwartz LW, Roy RV. Modeling draining flow in mobile and immobile soap films. J Coll Interf Sc 1999;218:309–23.
[40] Vitry Y, Dorbolo S, Scheid B. Antibubble generator. URL https://youtu.be/l49BoJCcf_I; Dec 2014.
[41] Battino R, Rettich TR, Tominaga T. The solubility of nitrogen and air in liquids. J Phys Chem Ref Data Monogr 1984;13(2):563.
[42] Stubenrauch C, Rojas OJ, Schlarmann J, Claesson PM. Interactions between nonpolar surfaces coated with the nonionic surfactant hexaoxyethylene dodecyl ether C12e6 and the origin of surface charges at the air/water interface. Langmuir 2004;20(12):4977–88.
[43] Fainerman VB, Lylyk SV, Aksenenko EV, Makievski AV, Petkov JT, Yorke J, et al. Adsorption layer characteristics of triton surfactants: 1. Surface tension and adsorption isotherms. Colloids Surf A Physicochem Eng Asp 2009;334:1–7.
[44] Wantke K-D, Fruhner H, Fang J, Lunkenheimer K. Measurements of the surface elasticity in medium frequency range using the oscillating bubble method. J Colloid Interface Sci 1998;208(1):34–48.

[45] Cheng N-S. Formula for the viscosity of a glycerol? Water mixture. Ind Eng Chem Res 2008;47:3285–8.
[46] Volk A, Kähler CJ. Density model for aqueous glycerol solutions. Exp Fluids 2018;59(5):75.
[47] Bhamla MS, Giacomin CE, Balemans C, Fuller GG. Influence of interfacial rheology on drainage from curved surfaces. Soft Matter 2014;10:6917–25.
[48] Matsumoto Y, Uda T, Takagi S. The effect of surfactant on rising bubbles. In: Balachandar S, Prosperetti Ae, editors. IUTAM symposium on computational approaches to multiphase flow. fluid mechanics and its applications. Dordrecht: Springer; 2006. p. 311–21.
[49] Allen H. On the motion of a sphere in a viscous fluid. Phil Mag 1900;50:323–38.
[50] Turton R, Levenspiel O. A short note on the drag correlation for spheres. Powder Technol 1986;47:83–6.
[51] Brown P, Lawler DF. Sphere drag and settling velocity revisited. J Environ Eng 2003;129:222–31.
[52] Israelachvili J. Intermolecular and surface forces. . 3rd ed.Amsterdam: Academic Press; 2011.
[53] Denkov ND, Marinova KG, Tcholakova SS. Mechanistic understanding of the modes of action of foam control agents. Adv Colloid Interface Sci 2014;206:57–67.
[54] Sánchez A Evangelio. Generacion controlada de microburbujas y microemulsiones. Estabilidad de burbujas en interfases. PhD Thesis Universidad de Sevilla; 2016.
[55] Tittarelli A, Borgini A, Bertoldi M, De Saeger E, Ruprecht A, Stefanoni R, et al. Estimation of particle mass concentration in ambient air using a particle counter. Atmos Environ 2008;42:8543–8.
[56] Morawska L, He C, Hitchins J, Gilbert D, Parappukkaran S. The relationship between indoor and outdoor airborne particles in the residential environment. Atmos Environ 2001;35:3463–73.
[57] Charles G, Mason S. The coalescence of liquid drops with flat liquid/liquid interfaces. J Colloid Sci 1960;15(3):236–67.
[58] Dorbolo S. Antibubble observed with monochromatic light (bottom view). URL https://youtu.be/JtrTpEmJZsA; Nov 2009.
[59] Mysels KJ, Shinoda K, Frankel S. Soap films: studies of their thinning and a bibliography. New York: Pergamon; 1959.
[60] Bruinsma R. Theory of hydrodynamic convection in soap films. Physica A: Statistical Mechanics and its Applications 1995;216(1):59–76.
[61] Kamp J, Villwock J, Kraume M. Drop coalescence in technical liquid/liquid applications: a review on experimental techniques and modeling approaches. Rev Chem Eng 2017;33(1):1–47.
[62] Lorenceau E, Quéré D, Eggers J. Air entrainment by a viscous jet plunging into a bath. Phys Rev Lett 2004;93(25):254501.
[63] de Gennes P-G, Brochart-Wyart F, Quéré D. Gouttes, Bulles, Perles et Ondes Belin (Paris) ; 2005.
[64] Quéré D. Fluid coating on a fiber. Annu Rev Fluid Mech 1999;31(1):347–84.
[65] Charru F. Hydrodynamic instabilities. Cambridge University Press; 2011.